Millimetre-wave measurements of the bulk magnetoconductivity of anisotropic metals: application to the organic superconductors κ-(BEDT-TTF)$_2$Cu(NCS)$_2$ and β"-(BEDT-TTF)$_2$SF$_5$CH$_2$CF$_2$SO$_3$ (BEDT-TTF≡bis(ethylene-dithio)tetrathiafulvalene)

2001 J. Phys.: Condens. Matter 13 2235

(http://iopscience.iop.org/0953-8984/13/10/317)

INSTITUTE OF PHYSICS PUBLISHING JOURNAL OF PHYSICS: CONDENSED MATTER

J. Phys.: Condens. Matter **13** (2001) 2235–2261 www.iop.org/Journals/cm PII: S0953-8984(01)17937-3

Millimetre-wave measurements of the bulk magnetoconductivity of anisotropic metals: application to the organic superconductors κ-(BEDT-TTF)$_2$Cu(NCS)$_2$ and β''-(BEDT-TTF)$_2$SF$_5$CH$_2$CF$_2$SO$_3$ (BEDT-TTF $\equiv$ bis(ethylene-dithio)tetrathiafulvalene)

J Marije Schrama[1], John Singleton[1,2,6], Rachel S Edwards[1], Arzhang Ardavan[1], Eva Rzepniewski[1], Rob Harris[1], Phi Goy[3], Michel Gross[3], John Schlueter[4], Mohamedally Kurmoo[1] and Peter Day[5]

[1] University of Oxford, Department of Physics, The Clarendon Laboratory, Parks Road, Oxford OX1 3PU, UK
[2] National High Magnetic Field Laboratory, Los Alamos National Laboratory, MS-E536, Los Alamos, NM 87545, USA
[3] AB Millimetre, 52, Rue Lhomond, 75005 Paris, France
[4] Chemistry and Materials Divisions, Argonne National Laboratory, 9700 South Cass Avenue, Argonne, IL 60439, USA
[5] The Royal Institution, Albemarle Street, London, UK

E-mail: j.singleton1@physics.ox.ac.uk

Received 11 October 2000

Abstract

We describe a novel resonant cavity system which allows the bulk magnetoconductivity of single crystals of anisotropic metals to be measured at GHz frequencies. The cavity can be made to rotate in a static magnetic field, permitting detailed studies of the dependence on the magnetic field orientation of the high-frequency magnetoconductivity. In this paper, the apparatus is used to measure the Fermi-surface topology of two organic superconductors; the details revealed are inaccessible to conventional fermiological techniques such as the de Haas–van Alphen effect. In κ-(BEDT-TTF)$_2$Cu(NCS)$_2$, Fermi-surface traversal resonances (FTRs) are observed. The angle dependence of the FTRs shows that the quasi-one-dimensional (Q1D) Fermi sheets of this material possess two distinct corrugations, with corrugation axes making angles of 17.3° and $-19.4°$ with the k_a-axis. Such data form important input parameters for current models of superconductivity in the organics, which invoke spin-density-wave-like fluctuations caused by partial nesting of the Q1D Fermi sheets. In β''-(BEDT-TTF)$_2$SF$_5$CH$_2$CF$_2$SO$_3$, cyclotron resonance is observed, along with its second and third harmonics. The detailed angle dependence of the intensities of the various cyclotron harmonics allows the elongation and orientation of the

[6] Author to whom any correspondence should be addressed.

closed section of the Fermi surface to be deduced, and strongly suggests that the interplane transport is coherent in this material. The effective mass deduced from the cyclotron resonance measurements is greater than that determined from magnetic quantum oscillations, in agreement with recent theoretical predictions.

(Some figures in this article are in colour only in the electronic version; see `www.iop.org`)

1. Introduction

Over the past decade, anisotropic metals and quasimetals have formed an increasingly important research area within condensed-matter physics [1]. Amongst these systems, one can include the 'high-T_c' cuprate superconductors [2], the layered ruthenates [3, 4] and manganites [5], and charge-transfer salts (crystalline organic molecular metals) [6]. In such systems, it is important to be able to characterize the interactions and many-body effects which affect the charge carriers [6–8]. It is also necessary to be able to check whether Fermi-liquid theory is applicable, what the detailed topology of the Fermi surface is (if it exists), and whether the band structure is coherent in all three dimensions [9].

Taking one example, there is considerable debate over the nature of superconductivity in quasi-two-dimensional charge-transfer salts [6, 10–12]. Several theories [13–16] stress the importance of the details of the Fermi-surface topology in providing suitable prerequisites for superconductivity. There is strong evidence that in many of these salts, the superconductivity is d-wave-like and mediated by spin-density-wave-like fluctuations [6, 10]; however, if the Fermi-surface geometry and interactions are altered slightly, it appears that BCS-like s-wave superconductivity *may* be the dominant low-temperature ground state [6]. Clearly it is essential to be able to measure fine details of the Fermi-surface topology in such materials [14].

In this paper, we give the first detailed description of a novel experimental technique for measuring the magnetoconductivity of anisotropic and layered materials at GHz frequencies. The technique is novel because it measures the high-frequency *bulk* conductivity of a metallic system; moreover, the use of a resonant cavity which rotates in the quasistatic magnetic field allows the detailed angle dependence of the conductivity to be mapped out. The technique has already led to the first definitive observations of cyclotron resonance in narrow-bandwidth metallic systems [6]; when compared to de Haas–van Alphen data, such experiments give information about the many body effects [6, 8, 17]. It has also been used to observe a new type of magneto-optical resonance, the Fermi-surface traversal resonance (FTR) [18, 19]. The observation of FTRs enables details of the Fermi-surface topology which are inaccessible to other methods to be mapped [6]. Finally, the apparatus has permitted the observation of a new type of cyclotron-resonance-like phenomenon in Sr_2RuO_4 [4]. In the present paper, we conclude with very recent data for two organic superconductors which illustrate the experimental technique and some of the phenomena mentioned above.

2. The experimental method

2.1. Millimetre-wave vector network analyser (MVNA)

The experimental technique is based around the millimetre-wave vector network analyser (MVNA) which acts as a tunable source and detector of GHz radiation [20]. A schematic diagram of the MVNA is shown in figure 1. The MVNA is based on two YIG (yttrium–iron-garnet) oscillators (master and slave) which are continuously tunable between 8 and

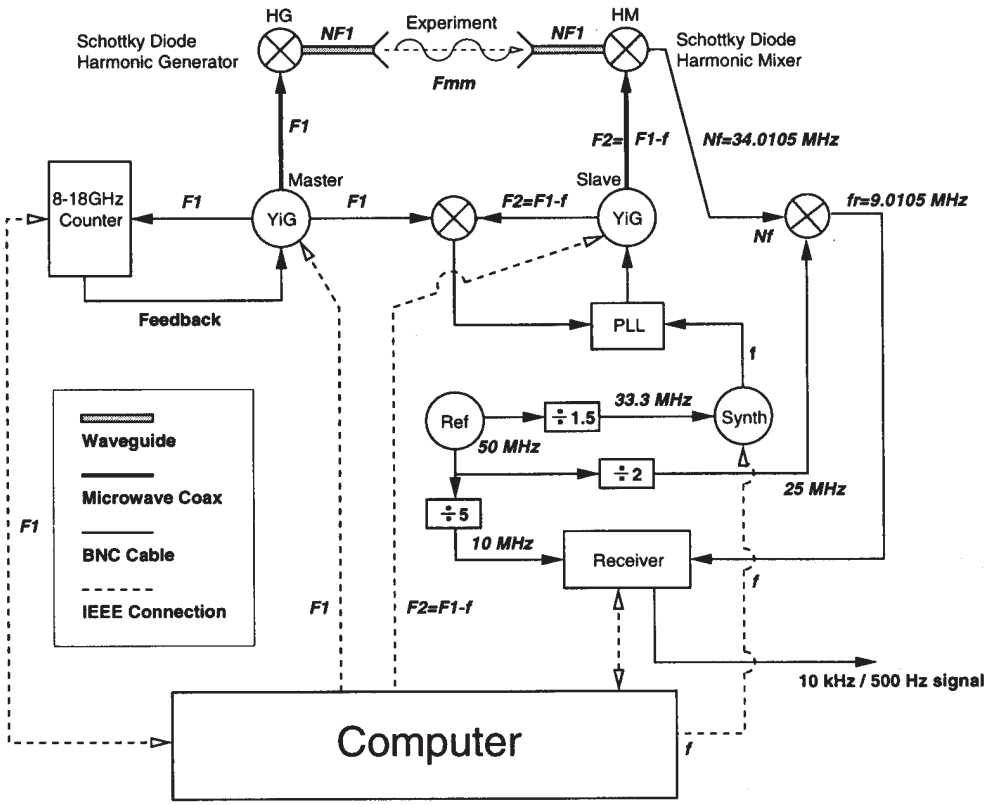

Figure 1. A schematic diagram of the millimetre-wave vector network analyser (MVNA) [20] (Synth = synthesizer, PLL = phase-locked loop, YIG = yttrium–iron-garnet oscillator, Ref = reference source, HG = harmonic generator, HM = harmonic mixer). For an explanation of the various frequencies, see the text.

18 GHz. The YIG oscillators are phase locked and the slave YIG follows the frequency of the master.

The master YIG is set at a frequency ($F1$) between 8 and 18 GHz, chosen by the user (see figure 1); the slave oscillates at $F2 = F1 - f$, where the offset frequency f is controlled by the computer. The oscillating current from the master YIG ($F1$) is sent to a Schottky diode (the harmonic generator (HG)) which acts as a transducer, emitting electromagnetic waves which are sent to the experiment. Owing to its non-linear current–voltage characteristic, the HG Schottky diode generates a comb of frequencies which are multiples of $F1$, $F_{\mathrm{mm}} = N \times F1$ with $N = 1, 2, 3, \ldots$.

The signal from the slave is sent to a second Schottky diode, the harmonic mixer (HM). The HM mixes the millimetre-wave signal received from the experiment ($F_{\mathrm{mm}} = N \times F1$) with the signal from the slave ($N' \times F2 = N' \times (F1 - f)$) to give frequencies

$$F_{\mathrm{mix}} = NF1 \pm N'(F1 - f). \tag{1}$$

The low-frequency interference signal ($N \times f$), generated by the mixing of millimetre waves with $N = N'$, is detected at a chosen harmonic N, i.e. the frequency is downconverted. $N \times f$ is equal to 34.010 488 MHz for all harmonics higher than 3 and 9.010 488 MHz for the harmonics $N = 1, 2$ and 3.

The amplitude of the detected signal ($F_{\mathrm{mix}} = N \times f$) is proportional to the amplitude of F_{mm} entering the HM (i.e. the signal from the experiment). Moreover, the phase of the signal from the experiment is preserved;

$$\phi_{\mathrm{mix}} = N\phi_1 + \delta\phi - N'\phi_2. \tag{2}$$

Here ϕ_{mix} is the phase of the detected signal, ϕ_1 and ϕ_2 are the phases of the master and the slave YIG respectively, and $\delta\phi$ is the phase shift due to the experiment.

In the vector receiver of the MVNA, F_{mix} is downconverted by mixing with signals derived from the same main reference source in order to keep the phase information. The final output signals are at 10 kHz and 500 Hz; both can be used with a lock-in amplifier or displayed on an oscilloscope.

In addition to the advantages of measuring both phase and amplitude from an experiment, the MVNA covers a very interesting range of energy in condensed-matter physics. With suitable extensions, the MVNA is tunable from 8 to 350 GHz continuously, and up to 800 GHz over a series of narrow bands [20,21]. These frequencies correspond to energies from 0.03 meV to 3 meV, or temperatures from 0.4 to 40 K. These are the characteristic energy scales of many phenomena in condensed-matter physics, including many-body effects in correlated-electron systems [6, 22] and Kondo insulators [23], and superconducting gaps in e.g. heavy-fermion [22] and organic superconductors [12]. Moreover, the frequencies correspond to cyclotron resonance at standard laboratory fields in organic molecular metals [6] and strongly interacting carrier systems [24].

The MVNA is therefore a very interesting source/detector combination for condensed-matter physics experiments. However, it is also very useful as a diagnostic instrument; frequency sweeps enable behaviour of the experiment to be analysed and optimized at all stages, so unhelpful phenomena such as parasitic millimetre-wave leaks and standing waves can be eliminated.

2.2. Bulk conductivity measurements of single crystals at GHz frequencies

High-frequency measurements of the conductivity of metallic crystals are usually limited by skin-depth effects [25]. However, the anisotropic or layered systems which are of interest in the current context usually consist of highly conductive planes which are relatively weakly coupled in the interplane direction; the interplane conductivity is therefore much lower (see figure 2). In the current experiments, the highly conducting planes of the sample are aligned parallel to the oscillating magnetic field $\boldsymbol{B}_{\mathrm{osc}}$ of the GHz radiation (see figure 2). The oscillating magnetic field induces circulating ac currents (J_{osc}), which Maxwell's equations dictate must flow in both interplane and in-plane directions. The low interplane conductivity restricts the size of current which can flow, so the skin depth can become very large [18, 26, 27]. Table 1 shows some examples of calculated skin depths; the relevant quantities for the current experiments are those listed against $\perp$, which are typically 100s of μm. As the typical sizes of the single crystals used in these experiments are $\sim 0.5 \times 0.5 \times 0.05$ mm^3 [18], the bulk of the crystal is penetrated as long as the induced currents are made to flow in the interplane direction.

The conductivity anisotropy dictates that the power absorbed by the sample is almost entirely due to the currents induced in the interplane direction; thus, it is mainly the interplane ac magnetoconductivity that is probed [18, 21, 26–28].

Figure 2 also shows a quasistatic magnetic field $\boldsymbol{B}$ that is applied. In most experiments the sample is tilted so that $\boldsymbol{B}$ makes an angle θ with the normal to the highly conducting planes; this involves rotating the cavity *and* sample with respect to $\boldsymbol{B}$ (see section 2.6). A further degree of freedom is given by the angle shown as ϕ, which defines the direction of

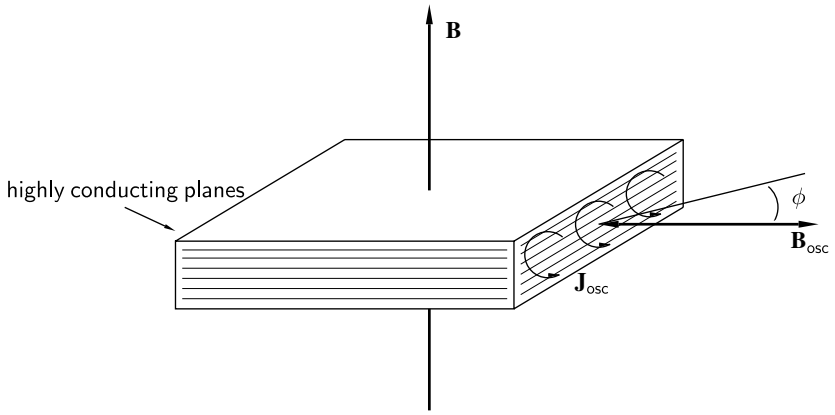

Figure 2. A schematic diagram of the configuration required for measuring a layered metallic system; the oscillatory magnetic field of the GHz radiation $\boldsymbol{B}_{osc}$ is applied in the highly conducting planes. The induced currents $\boldsymbol{J}_{osc}$ must flow in both in-plane and interplane directions. In the experiments described subsequently, a quasistatic magnetic field $\boldsymbol{B}$ is applied; in the figure it is shown perpendicular to the sample's highly conducting planes. However, in most of the experiments the sample is tilted so that $\boldsymbol{B}$ makes an angle θ with the normal to the highly conducting planes. The angle ϕ defines the direction of $\boldsymbol{B}_{osc}$ with respect to one of the in-plane crystal axes.

Table 1. Typical normal-state conductivities (σ) and skin depths (δ) of two organic conductors which have been studied using the techniques described in this paper; the experiments on κ-(BEDT-TTF)$_2$Cu(NCS)$_2$ are described later in this paper, and those on α-(BEDT-TTF)$_2$KHg(SCN)$_4$ are in reference [18]. The skin depths have been calculated for a frequency of 70.7 GHz. The notation '$\|$' is used to indicate the direction of the induced currents parallel to the conducting planes, '$\perp$' refers to the direction of the induced ac currents normal to the conducting planes. The 'reference' column gives the source for the conductivity data.

		σ (Ω m)$^{-1}$	δ (μm)	T (K)	Reference
κ-(BEDT-TTF)$_2$Cu(NCS)$_2$	$\|$	4×10^5	3	10	[29]
	$\perp$	4.0×10^2	95	10	[29]
α-(BEDT-TTF)$_2$KHg(SCN)$_4$	$\|$	2.5×10^4	12	1	[30]
	$\perp$	12.5	500	1	[30]

$\boldsymbol{B}_{osc}$ with respect to one of the in-plane crystal axes[7]. In this way, the angle dependence of the high-frequency magnetoconductivity can be mapped [31].

In order that $\boldsymbol{B}_{osc}$ is always applied in the highly conducting planes of the sample, a rectangular resonant cavity system is used. This offers two advantages. Firstly, the measurement sensitivity is greatly enhanced; the sample is part of the resonator and therefore changes in the sample's properties have a large effect on properties of the resonator. This is crucial in studying very small single crystals [18, 21]. Secondly, the electromagnetic environment inside the cavity is well known and largely independent of temperature, magnetic field, or sample properties as long as the sample is small.

This is in sharp contrast to e.g. a transmission experiment at GHz frequencies [32–34]. In transmission experiments, the sample is exposed to a random mixture of oscillating electric

[7] Because of the construction of the rotation mechanism and the polarization of the millimetre waves within the resonant cavity (see below), this also has the effect of fixing the plane of rotation of the sample with respect to $\boldsymbol{B}$ [18].

and magnetic fields and the thermal contraction of the waveguide and the changing sample properties vary the standing-wave pattern. Hence the field distribution around the sample may change during the measurement.

2.3. Rectangular cavity modes

Although cylindrical cavities are simpler to manufacture and higher Q-factors are achieved [35], rectangular cavities have a number of very important advantages. The rectangular cavity has robust modes which are widely separated in frequency; therefore the mode mixing, caused by a sample perturbing the field distribution in the cavity, is very small compared to that in cylindrical cavities [35]. Secondly, for a given frequency, a rectangular cavity is more compact; this is of advantage when it comes to rotating the cavity in the magnetic field.

The modes of a rectangular cavity are readily derived with good accuracy by making the assumption that the cavity walls are perfect conductors [36]; the transverse electric (TE) modes are

$$E_x \propto \cos(k_x x)\sin(k_y y)\sin(k_z z) \qquad B_x \propto \sin(k_x x)\cos(k_y y)\cos(k_z z) \tag{3}$$

$$E_y \propto \sin(k_x x)\cos(k_y y)\sin(k_z z) \qquad B_y \propto \cos(k_x x)\sin(k_y y)\cos(k_z z) \tag{4}$$

$$E_z = 0 \qquad B_z \propto \cos(k_x x)\cos(k_y y)\sin(k_z z). \tag{5}$$

For a cavity with dimensions a, b, and d in the x-, y-, and z-directions respectively, the allowed wavevectors are $k_x = m\pi/a$, $k_y = n\pi/b$, and $k_z = p\pi/d$, where m, n, and p are the numbers of half-wavelengths in the standing waves of the cavity. Such a mode is denoted TE_{mnp}, and the resonant frequencies are given by [35, 36]

$$f_0 = \frac{1}{2}\sqrt{\frac{(m/a)^2 + (n/b)^2 + (p/d)^2}{\mu\epsilon}} \tag{6}$$

where ϵ is the permittivity and μ is the permeability of whatever fills the space within the cavity (usually vacuum).

The distribution of the electric (E) and magnetic (B) fields of the TE_{102} cavity mode is shown in figure 3; this is the chief mode used in the experiments described below. Note that there is a magnetic field antinode at the centre of the cavity in which the sample is placed.

2.4. Practical cavity design

A schematic diagram of the resonant cavity used in the experiments is shown in figure 4. The body of the cavity is constructed from a piece of silver WG26 waveguide with inner dimensions $1.55 \times 3.10 \times 6.00$ mm^3. The two open ends of the body are closed with stainless-steel top plates, which screw onto brass lugs soldered to the body. Silver foil (thickness ~ 100 μm) is fitted between the top plates and the cavity. The cavity's body is made slightly larger than the supporting lugs to ensure that the silver foil is pressed firmly against the cavity body, as the currents induced in the TE_{102} mode cross all the faces of the cavity [35]; good electrical contact is important to minimize the dissipation of the induced high-frequency currents in the walls.

Substituting the dimensions of the cavity into equation (6) yields 70 GHz for the TE_{102} mode. Figure 5 shows the cavity transmission of a loaded rectangular cavity versus frequency recorded using the MVNA. One frequency sweep is taken at room temperature (open diamonds) and the other frequency sweep is taken at 1.4 K (full circles). The measured resonant frequency at the lower temperature is 70.81 GHz, in good agreement with the calculated frequency. The magnitude of the low-temperature resonance is larger than the room-temperature resonance,

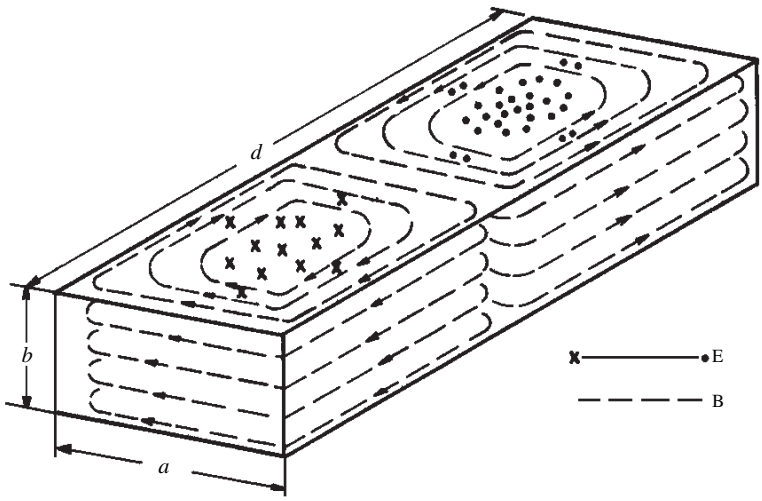

Figure 3. The field distribution for the TE_{102} mode of a rectangular cavity. $\boldsymbol{E}$ represents the oscillating $\boldsymbol{E}$-field, and $\boldsymbol{B}$ represents the oscillating $\boldsymbol{B}$-field. (After reference [35].)

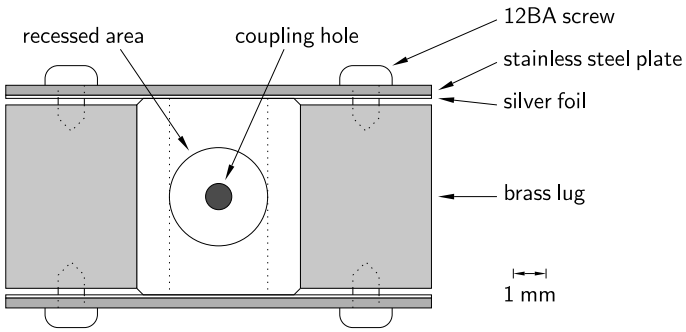

Figure 4. A schematic diagram of the rectangular cavity used in the experiments. The white section in the centre is the silver WG26 waveguide.

showing that the silver cavity walls and sample dissipate less power at low temperature because of their improved conductivity. The resonance position shifts up in frequency on lowering the temperature as a result of a slight thermal contraction of the cavity.

The TE_{101} and TE_{104} modes have the same coupling configuration as the TE_{102} mode. The TE_{101} mode has an oscillating electric field antinode in the centre of the cavity and the TE_{102} mode has a oscillating magnetic field antinode in the centre. Therefore by positioning the sample in the centre of the cavity it can be exposed to both electric and magnetic fields in the same cavity [26]. In figure 5(b) the fundamental mode TE_{101} is observed at 56.4 GHz.

2.5. Coupling in the radiation

The coupling holes allow the millimetre wave to enter the cavity and are positioned at the centres of both ad-planes (see figure 3). There is a fine balance between a hole large enough to enable sufficient millimetre waves to enter the cavity, and a hole small enough to keep radiation losses small. The optimal condition for coupling is $\lambda >$ diameter $> w$ [35], where λ is the

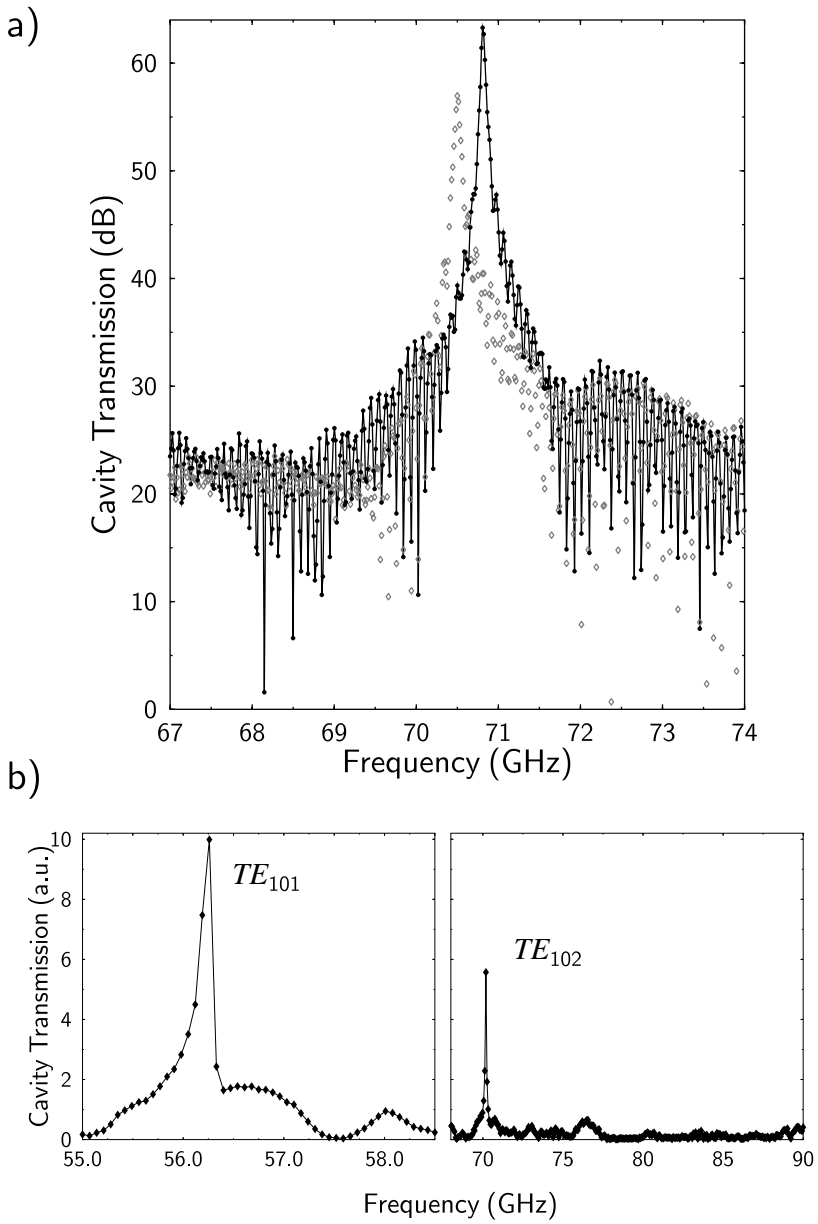

Figure 5. The frequency response of the rectangular cavity loaded with a charge-transfer salt crystal. (a) The TE_{102} resonance in dB. The open diamonds are data taken at room temperature and the full circles are 1.4 K data. (b) The TE_{101} resonance (left) and the TE_{102} resonance (right), in linear units.

wavelength and w the wall thickness. Careful testing showed the optimal hole diameter to be 0.8 mm in the cavity shown in figure 4. To reduce losses in the cavity wall the area around the hole is recessed, as shown in figure 4 and figure 6.

Figure 6 shows how the cavity is placed between the waveguides which connect it to the HG and HM heads; for simplicity, the rotation mechanism (see section 2.6) has been

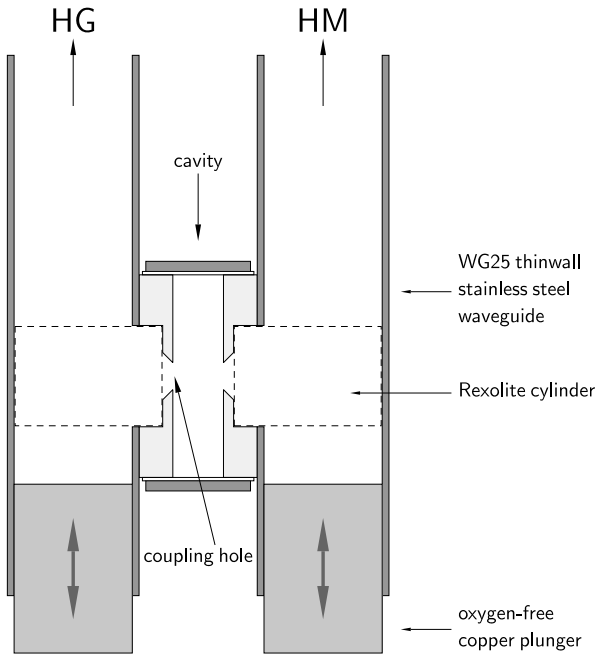

Figure 6. A schematic diagram of the vertical cross-section of the rectangular cavity placed between the two waveguides to the source (HG) and detector (HM). The mechanism for rotating the cavity (see section 2.6) has been omitted for clarity.

omitted. The cavity is held in this position by two Rexolite cylinders of 3 mm diameter which are fitted in the recessed area around the coupling holes and which extend through the holes (3 mm diameter) in the waveguides. From our tests, Rexolite appears to be very transparent to millimetre waves and non-magnetic.

To couple effectively to a cavity, the electromagnetic wave distribution in the waveguide next to the coupling hole should emulate the electromagnetic wave distribution inside the cavity next to the holes [35]. For example, the TE_{102} mode has an oscillating magnetic field maximum at the position of the holes (see figure 3). Consequently the mode in the waveguides should also have an oscillating magnetic maximum at the hole. The waveguides are terminated with oxygen-free copper plungers plated with gold; millimetre waves are reflected by the plungers and standing waves are set up in the waveguides. By moving the plungers in or out of the waveguides, the wave distribution can be adjusted to maximize the coupling to the cavity.

Note that in figure 5(a) the cavity transmission oscillates rapidly when the frequency is changing. This is because, while sweeping the frequency, the wavelength of the millimetre waves changes continuously; thus, waves in the waveguides interfere constructively and destructively in alternation.

2.6. Rotating the cavity

Once the sample is placed in the resonator it becomes part of it and therefore the sample cannot be moved without disturbing the surrounding electromagnetic environment. Moreover, the large-skin-depth regime in anisotropic metallic samples depends on keeping the oscillating magnetic field *within* the sample's highly conducting planes (see section 2.2). Therefore, in order to perform studies of the sample's response to the orientation of a steady magnetic

field, the sample and cavity must be rotated in the steady magnetic field together. This is accomplished in a special cryogenic insert (outer diameter 14.5 mm) designed for ^{3}He and ^{4}He cryostats which fit inside a 17 T superconducting magnet in Oxford or the 33 T Bitter coils at NHMFL Tallahassee.

The key mechanism in the insert consists of a worm drive and a gear wheel. The cavity is made to fit tightly inside a rectangular hole in the wheel; the worm which turns the wheel is driven by a rod from the top of the insert (see figure 7) which allows one to rotate the cavity and sample in the cryostat at cryogenic temperatures. The worm is held gently on the wheel by a small spring which is just visible in figure 7.

Figure 7. Detail of the cryogenic insert designed to rotate the rectangular resonant cavity and sample in a quasistatic magnetic field. The rectangular cavity is visible within the brass cogwheel; it pivots about the Rexolite cylinders which also couple the cavity to the waveguides (see figure 6). The worm drive which turns the cogwheel is at the top of the picture. The wedge that clamps the cavity tightly between the waveguides is just visible behind the rearmost waveguide.

To avoid millimetre-wave leaks, the cavity is clamped tightly between the two waveguides. The clamp consists of a wedge sliding in a tapering groove. On pulling the wedge up using a screw micrometer at the top of the insert, the cavity is free to rotate; on pressing the wedge down, the cavity is fixed and ready for a measurement.

Note that rotating the cavity decreases the coupling to the waveguides as $\cos^2\theta$, where θ is the angle of rotation of the cavity with respect to the waveguides [35]; in practice this tends to restrict measurements to $|\theta| \leqslant 75^\circ$.

2.7. Other considerations

A resonant cavity is a damped oscillator for electromagnetic waves. Waves are (partly) reflected at the cavity's highly conducting walls and form standing-wave patterns (modes) inside the resonator. The energy losses from the cavity are chiefly due to dissipation via induced currents in the walls, losses through the coupling holes, and absorption of the millimetre waves by the sample. They are expressed in terms of the Q-factor of the cavity

$$Q = \omega_0 \frac{\text{stored energy}}{\text{power loss per cycle}} = \frac{\omega_0}{\Gamma} \tag{7}$$

where ω_0 is the resonant angular frequency and Γ is full angular frequency width at half-maximum of the resonance. The contributions to the dissipation sum such that

$$1/Q = 1/Q_{\text{walls}} + 1/Q_{\text{coupling}} + 1/Q_{\text{sample}} \tag{8}$$

where the subscripts indicate the source of the dissipation.

Damped oscillators are treated in many texts (see e.g. reference [36]); the amplitude A and phase Φ of the E- and B-fields of the electromagnetic waves in the cavity are given by

$$|A(\omega)|^2 = \frac{A_0^2}{(\omega_0/2Q)^2 + (\omega - \omega_0)^2} \tag{9}$$

and

$$\Phi = -\arctan\left(\frac{2(\omega - \omega_0)}{\omega_0/2Q}\right) \tag{10}$$

where A_0 is the notional amplitude of the field supplying energy to the cavity and Φ is measured relative to this field.

In experiments the millimetre-wave frequency is always set at the resonant frequency of the (loaded) cavity. There are two ways to accomplish this.

(1) Lock the MVNA frequency at the resonant frequency of the cavity [18,21]. The frequency counter (EIP575) is set at a reference frequency chosen by the user. The frequency of the master YIG is fed into the frequency counter. The counter compares the two frequencies and corrects the difference by sending a voltage proportional to the frequency difference into the frequency-stabilization input of the YIG (see figure 1). This feedback loop stabilizes the frequency to within 100 Hz, the accuracy of the frequency counter. This method can be used only if changes in the sample properties are small throughout a measurement, i.e. $\Delta\omega_0 \ll \Delta\Gamma$, where ω_0 is the resonance frequency and Γ the resonance width at half-maximum, and the symbol Δ indicates small changes in these quantities.

(2) Phase lock the cavity at resonance [28]. The phase changes very rapidly around the resonance frequency but remains constant at resonance, even if the resonant frequency changes (see equation (10)). The MVNA final output signal (500 Hz or 10 kHz) is sent to an external lock-in amplifier; the out-of-phase output of the lock-in is connected to the stabilization input of the YIG. If the resonant frequency of the cavity changes, the out-of-phase output of the lock-in amplifier sends a feedback voltage to the YIG, and this tunes the frequency back to the resonant frequency. This method is useful if the resonant frequency changes during the experiment. However, other components causing a phase drift must be carefully eliminated.

In all of the experiments reported in the current paper, method 1 is used, i.e. the angular frequency of the MVNA is fixed at a constant value ω.

2.8. What is measured in a resonant cavity?

In order to relate the measured cavity parameters (i.e. the change in amplitude and phase of the signal) to the sample properties, the amount of millimetre-wave penetration in the sample has to be assessed. At resonance ($\omega = \omega_0$), small changes in the resonance amplitude are proportional to changes in the Q-factor and inversely proportional to changes in the power dissipated (see equation (9)).

The phase is zero at resonance; when changes in the sample properties cause ω_0 to shift with respect to the fixed frequency ω, the change in phase is proportional to the change in resonant frequency (see equation (10)). If changes in resonance frequency are no longer small compared to the frequency width of the resonance (Γ), mixing between the phase and amplitude signal makes it impossible to treat the cavity parameters as independent. We now describe three types of limiting behaviour.

2.8.1. Depolarization regime. In the depolarization limit (skin depth $\delta \gg l$, where l is the sample size), the millimetre waves penetrate the sample completely. For a dielectric with complex permittivity $\epsilon = \epsilon' + \mathrm{i}\epsilon''$ placed in an oscillating electric field antinode, the change in amplitude (absorption) is directly proportional to the imaginary part of the permittivity ϵ'' and the change in phase signal (dispersion) is proportional to the real part of the permittivity ϵ' [37]. The absorption of electromagnetic waves in the sample is proportional to the polarizability of the sample [37].

If a magnetic material is placed in an oscillating magnetic field antinode, the change in amplitude of the signal is directly proportional to the imaginary part of the permeability μ'' and the change in phase is proportional to the real part of the permeability μ' [37].

2.8.2. Skin-depth regime. In the skin-depth limit ($\delta \ll l$), only the surface of the sample is probed by the millimetre waves and the property measured is the surface impedance Z_s [28],

$$Z_\mathrm{s} = R_\mathrm{s} + \mathrm{i}X_\mathrm{s} \tag{11}$$

where R_s denotes the surface resistance and X_s the surface reactance. Changes in R_s and X_s result in changes in the resonance width Γ and resonant frequency ω, given by

$$\frac{\pi\,\Delta\Gamma}{\omega_0} = \zeta\,\Delta R_\mathrm{s} \tag{12}$$

$$\frac{\Delta\omega}{\omega_0} = \zeta\,\Delta X_\mathrm{s} \tag{13}$$

where the symbol Δ represents a change in the quantity in question and ζ is a geometrical factor known as the resonator constant [35].

2.8.3. Anisotropic metals. In an anisotropic metal where the skin depth is larger than the sample size, the millimetre waves penetrate the whole sample. The sample experiences a constant change in magnetic field $\partial B/\partial t$ when placed in a magnetic field antinode. The oscillating magnetic field induces an electric field $\boldsymbol{E}$:

$$\frac{\partial \boldsymbol{B}}{\partial t} = -\boldsymbol{\nabla} \times \boldsymbol{E}. \tag{14}$$

Integrating over an area (A) and using Stokes's theorem gives

$$\int_{\text{surface}} (\boldsymbol{\nabla} \times \boldsymbol{E}) \cdot \mathrm{d}\boldsymbol{a} = \oint_{\text{line}} \boldsymbol{E} \cdot \mathrm{d}\boldsymbol{l} = \mathcal{E} = -A\frac{\partial \boldsymbol{B}}{\partial t} \tag{15}$$

where $\mathcal{E}$ is the electromotive force (emf). Therefore the oscillating magnetic field is proportional to the emf and the emf determines how much current flows in the loop surrounding A. The work done on a unit charge in one trip around the circuit is $-\mathcal{E}$; hence, the total work done per unit time is

$$\frac{\mathrm{d}W}{\mathrm{d}t} = -\mathcal{E}I \tag{16}$$

where I is the current. Because the magnetic field oscillates with a constant frequency the emf is constant (voltage driven) and this makes the current proportional to the conductivity of the material. The millimetre-wave power absorbed is caused by dissipation of the induced (eddy) currents. Therefore (and somewhat counterintuitively) an increase in the conductivity results in an increase of the induced currents and an increase of the power dissipated. Therefore small changes in the resonant amplitude of a cavity are inversely proportional to the changes in conductivity of the sample [26].

3. Application to the organic superconductor κ-(BEDT-TTF)$_2$Cu(NCS)$_2$

3.1. Introduction

The family of superconducting charge-transfer salts κ-(BEDT-TTF)$_2$X, where X can, for example, be Cu(NCS)$_2$, Cu[N(CN)$_2$]Br, or I_3, has attracted considerable attention (for a review see section 3 of reference [6]). There is considerable evidence that the superconductivity in these salts is not due to the conventional BCS, phonon-mediated mechanism (see references [6, 10, 12] and references therein); however, the salts have well-defined quasi-two-dimensional Fermi surfaces, indicating that the quasiparticles can be described by Fermi-liquid theory at low temperatures [6].

Of all the κ-phase salts, κ-(BEDT-TTF)$_2$Cu(NCS)$_2$ ($T_c = 10.4$ K) is perhaps the most extensively studied. The Fermi surface is shown schematically in figure 8; it consists of a pair of electron sheets and a quasi-two-dimensional hole cylinder.

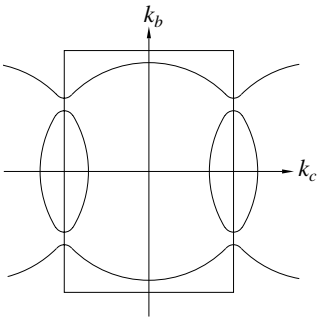

Figure 8. An in-plane cross-section of the Fermi surface of κ-(BEDT-TTF)$_2$Cu(NCS)$_2$ [44].

The theories derived to describe superconductivity in the κ-phase BEDT-TTF salts generally assume that the superconductivity is mediated by spin-density-wave-like fluctuations [13–16]; they are based on a detailed knowledge of the Q1D sheets of the Fermi surface and in particular their ability to nest. Whilst the Q2D Fermi-surface section of κ-(BEDT-TTF)$_2$Cu(NCS)$_2$ is well known, both from experimental data (Shubnikov–de Haas (SdH) [38–42] and de Haas–van Alphen (dHvA) effects [43]) and from band-structure calculations [44, 45], little is known about the precise topology of the Q1D sheets. Breakdown and quantum-interference frequencies [39] provide a proof of the existence of Q1D Fermi-surface sections and, more recently, angle-dependent magnetoresistance oscillations (AMRO) [46, 47] were used to measure the Q1D Fermi sheets. The orientation of the Q1D sheets in the crystal is known from the AMRO data but no detailed information on the topology of the Q1D sheets could be deduced.

By contrast, using the millimetre-wave techniques described in this paper, two interplane warping components of the Q1D Fermi sheets have been revealed. The experiment described below shows that the directions of the corrugations of the Fermi sheet are 17.3° and -19.4° with respect to the reciprocal k_a-axis. The experiments involve the observation of a phenomenon known as the *Fermi-surface traversal resonance* [18, 19], which will be described in the following section.

3.2. Fermi-surface traversal resonance

The motion of the quasiparticles in a magnetic field $\boldsymbol{B}$ is determined by the equation for their group velocity $\boldsymbol{v}$:

$$\hbar \boldsymbol{v} = \boldsymbol{\nabla}_{\boldsymbol{k}} E(\boldsymbol{k}) \tag{17}$$

where $E(\boldsymbol{k})$ and $\boldsymbol{k}$ are the quasiparticle energy and wavevector respectively and $\boldsymbol{\nabla}_{\boldsymbol{k}}$ the gradient operator in wavevector space, and by the Lorentz force [48]

$$\hbar \frac{\mathrm{d}\boldsymbol{k}}{\mathrm{d}t} = -e\boldsymbol{v} \times \boldsymbol{B}. \tag{18}$$

These equations show that the component of $\boldsymbol{k}$ parallel to $\boldsymbol{B}$ remains constant, and that the quasiparticle energy remains constant; i.e. the k-space path of the quasiparticle is defined by the intersections of surfaces of constant energy (such as the Fermi surface) with planes perpendicular to $\boldsymbol{B}$ [48].

Figure 9 represents the path of a quasiparticle across a simple Q1D Fermi-surface sheet with one sinusoidal corrugation; its velocity (always perpendicular to the Fermi surface—see equation (17)) is represented by arrows. For a general direction of the in-plane magnetic field ($\psi \neq 0$ in figure 9), the quasiparticle possesses an oscillating real-space velocity which depends on the shape of the Fermi surface; its velocity 'rocks' as it is driven across the corrugations. Semiclassical [6,18,49] and quantum-mechanical [6,19] arguments show that an electromagnetic wave, the frequency of which matches the frequency of the oscillating velocity component, couples to the oscillating velocity; hence, the quasiparticle motion contributes resonantly to the ac magnetoconductivity. The frequency of the oscillating real-space velocity can be measured and linked directly to the Fermi-surface shape. This phenomenon is known as the Fermi-surface traversal resonance (FTR) [18].

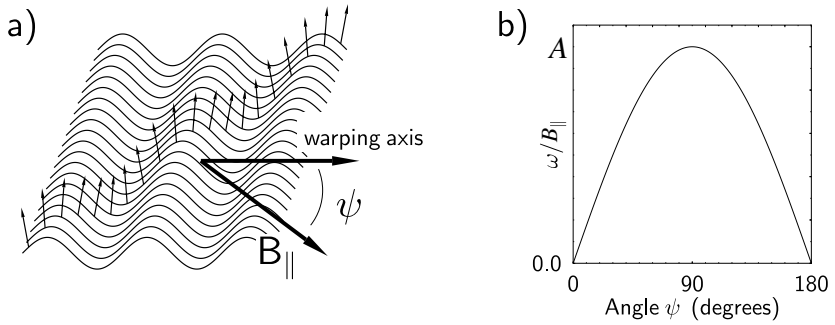

Figure 9. (a) A simple sinusoidal warped Fermi sheet with the magnetic field $\boldsymbol{B}_{\|}$ in the plane of the sheet. The magnetic field makes an angle ψ with the warping axis. (b) The magnetoconductivity resonance field as a function of angle ψ arising from the Fermi sheet shown in (a).

The rotation of the in-plane magnetic field $B_{\|}$ through an angle ψ makes the resonance frequency shift as $\sin\psi$ (see figure 9(b)); at $\psi = 0$ the quasiparticle velocities do not oscillate; at $\psi = 90^{\circ}$ the frequency is a maximum [18] (see figure 9(a)).

The experiments described in this paper use a fixed frequency and sweep the magnetic field. Hence, the FTR's shift in field as a function of ψ [18] as follows:

$$\frac{\omega}{B_{\|}} = A\sin(\psi + \psi_0). \tag{19}$$

Here we have introduced the angle ψ_0 to indicate that the experimental coordinates may be offset with respect to the warping axis. It is the angle dependence given by equation (19) which enables FTRs to be identified. In a real Fermi surface, there may be several different types of corrugation; each corrugation will give rise to an FTR [18, 19].

In an experiment where the steady magnetic field is rotated with respect to the sample, it is usually not the case that the plane of rotation of the field coincides with the plane of the Fermi sheet, i.e. in general $\boldsymbol{B} \neq \boldsymbol{B}_{\|}$. Therefore we need to transform the experimental coordinates

($\boldsymbol{B}$, θ, and ϕ) into 'FTR' coordinates ($\boldsymbol{B}_\parallel$, ψ, and ψ_0). The experimental parameters are listed below.

- B is the magnetic field strength at the resonance.
- θ is the angle between the cavity (and sample) and the magnetic field, where $\theta = 0$ corresponds to the situation where the magnetic field is aligned along the least conducting direction of the sample (k_z). This alignment can be checked by measuring the frequency of the quantum oscillations in the ac response.
- ϕ is the azimuthal angle describing the plane of rotation of the sample in the magnetic field; it can be estimated from the crystallographic alignment of the sample and the known orientation of the Q1D Fermi sheets in the crystal. If the orientation is *not* known, data must be recorded at many azimuthal angles.

The magnetic field $\boldsymbol{B}$ is set to rotate in the k_xk_z-plane over angle θ (see figure 10). The Fermi sheet is defined in the ρ_xk_z-plane, with the field in the plane of the sheet $\boldsymbol{B}_\parallel$ making an angle ψ with the k_z-axis. ψ_0 is the angle that the corrugation of the Fermi sheet makes with the k_z-axis. Simple geometrical operations yield

$$B_\parallel = B\sqrt{\sin^2\theta\cos^2\phi + \cos^2\theta}. \tag{20}$$

and

$$\tan\psi = \tan\theta\cos\phi. \tag{21}$$

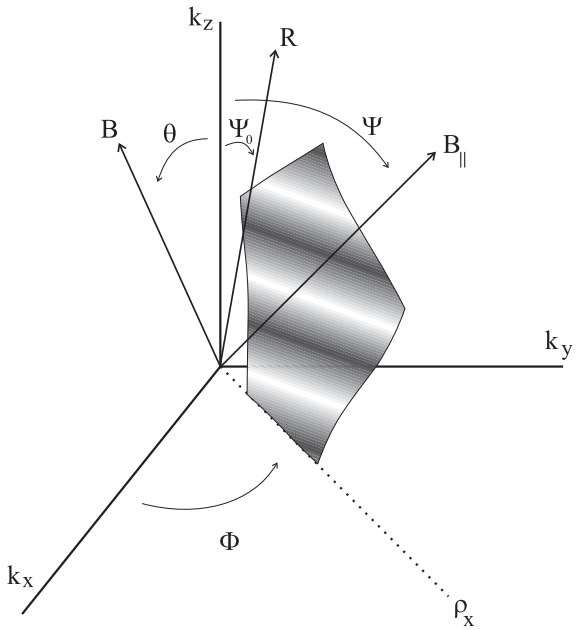

Figure 10. Definition of the angles used in the FTR experiment and analysis. The parameters from the experiment are θ, the cavity rotation angle, the azimuthal angle ϕ, and the magnetic field at the resonance $\boldsymbol{B}$. The 'FTR' parameters are the angle ψ, the magnetic field $\boldsymbol{B}_\parallel$ in the plane of the Fermi surface, and ψ_0, the tilting of the warping axis ($\boldsymbol{R}$) with respect to k_z.

The angle dependence of the FTRs in experimental parameters is obtained from equation (19) by substituting for $B_\parallel$ and ψ:

$$\frac{\omega}{AB} = \sqrt{\sin^2\theta\cos^2\phi + \cos^2\theta}\,\sin[\arctan(\tan\theta\cos\phi) + \psi_0]. \tag{22}$$

3.3. Raw data

Figure 11 shows raw cavity transmission data for a cavity loaded with a single crystal of κ-(BEDT-TTF)$_2$Cu(NCS)$_2$ (for preparation and purity details see references [50, 51]); data for three different cavity angles are shown. The data traces in figure 11 are normalized and offset for clarity. The normalization is to cancel out the difference in signal strength, as with increasing θ the coupling and therefore the cavity transmission signal decreases. The sample is placed in the centre of the cavity with the b-axis (k_b) aligned parallel to the oscillating magnetic field ($\phi = 90^\circ$); this also has the effect of defining the plane of rotation of the sample in the quasistatic magnetic field (see figures 6, 3, and 7).

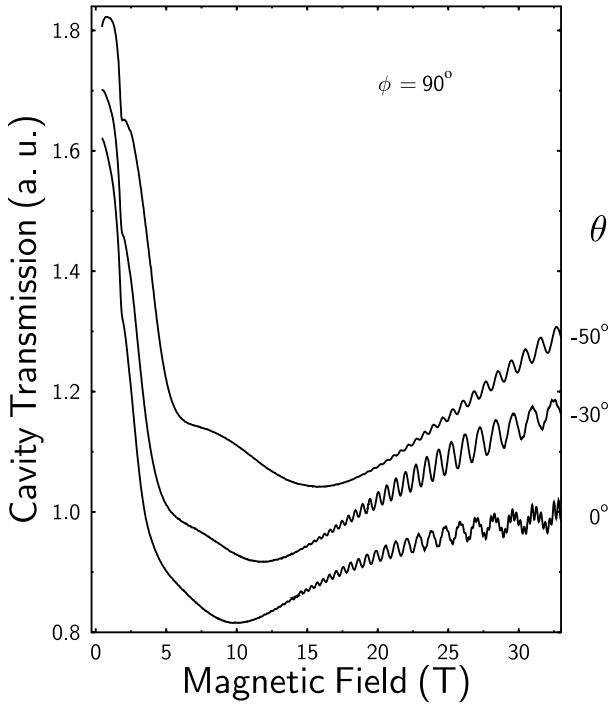

Figure 11. Transmission of the rectangular resonant cavity system loaded with a single crystal of κ-(BEDT-TTF)$_2$Cu(NCS)$_2$. The temperature is 1.5 K; the frequency is set to 70.895 GHz, the resonant frequency of the cavity. The sample's azimuthal angle is $\phi = 90^\circ$; data for three cavity angles, θ, are shown.

The data for $\theta = 0^\circ$ in figure 11 show a steep decrease in cavity transmission from 0 T to 2 T. The small shoulder around 1.8 T is a background feature attributed to the stainless-steel waveguides which is independent of temperature and present even in the absence of a sample. The large change in signal over this low-field range is associated with the properties of the mixed state [31, 52]. Around 3 T there is a feature associated with the transition from superconducting to normal, which has been attributed to a variety of mechanisms [31, 52]; at values of θ away from 90°, this feature follows the angle dependence of B_{c2}, moving as $\sim 1/\cos\theta$ [50] (see figure 11).

A wide resonance around 10 T is clearly visible at $\theta = 0$; at higher angles θ, the resonance shifts up in field. Above 13 T (at 1.5 K), magnetic quantum oscillations become visible; the quantum oscillations show that a pure sample has been used and allow the consistency

of the cavity angle and the sample orientation to be checked. The frequency (F) of the quantum oscillations increases at higher angles as $F = F_0/\cos\theta$, in line with expectations [6]. Above 25 T, higher-frequency magnetic breakdown and Shiba–Fukuyama–Stark quantum-interference oscillations are observed [6, 39, 53].

The position in the magnetic field of the resonance is plotted versus θ in figure 12. Figure 12(a) and figure 12(b) show data recorded at temperatures 1.5 K and 4.2 K respectively and demonstrate that there is little temperature dependence of the resonance position, although the resonance amplitude increases on lowering the temperature; any difference between the two data sets is probably due to slight differences in sample alignment since they were recorded on separate runs. The solid lines in figure 12 are fits to

$$\frac{1}{B} = \frac{1}{B_0}\sin(\theta + \theta_0) \tag{23}$$

(see equation (19)). Fits to the 1.5 K data in figure 12 give $1/B_0 = 0.083 \pm 0.002$ T^{-1} and $\theta_0 = 84.3^\circ \pm 2^\circ$. A single 'arch' of this form could be the result of a cyclotron resonance due to the closed Q2D pocket of the Fermi surface [6]. Alternatively, it might represent an FTR from a Q1D Fermi sheet with a single sinusoidal warping, either in the in-plane or interplane directions. In order to make the identification of the magneto-optical resonance unambiguous, data for several values of ϕ must be used.

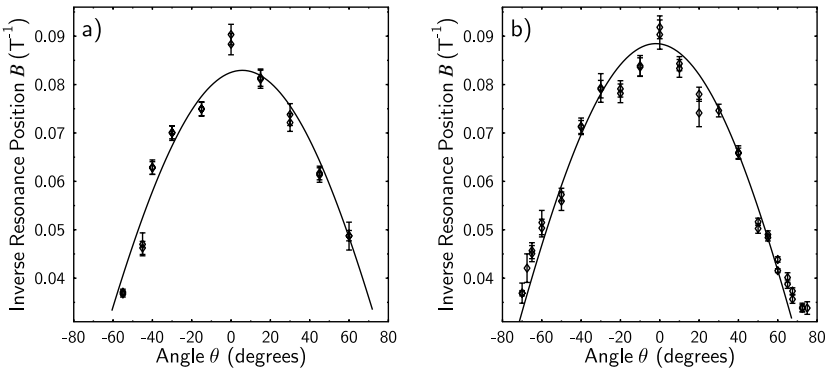

Figure 12. Resonance positions versus angle θ for azimuthal angle $\phi = 90^\circ$. (a) $T = 1.5$ K. (b) $T = 4.2$ K.

To determine the origin of the resonance, four azimuthal angles were measured, $\phi = 0^\circ$, 20°, 45°, and 90°. At $\phi = 0^\circ$ the oscillating magnetic field is parallel to the c-axis (k_c). The resonance positions for $\phi = 20^\circ$ are plotted in figure 13; it is immediately obvious that the angle dependence of the data differs from that of the $\phi = 90^\circ$ data in figure 12, strongly suggesting that the magneto-optical feature is not a cyclotron resonance.

To get a better picture of what is happening, the experimental coordinates must be transformed into 'FTR' coordinates (see equations (20) and (21)). However, the feature associated with the transition from superconducting to normal can act to obscure the magneto-optical resonance. In figure 13(a) the position of the feature, which follows B_{c2} in being proportional to $1/\cos\theta$ at low angles [6, 50, 51], is plotted as a solid line. Data for which the magneto-optical resonance and the superconducting feature interfere are removed from the 'FTR' coordinates plots. The transformed data are presented in figure 13(b). The transformation gives a much clearer picture of the data and two 'arches' are readily observed, indicating that two corrugations with different warping axes are present [6, 18].

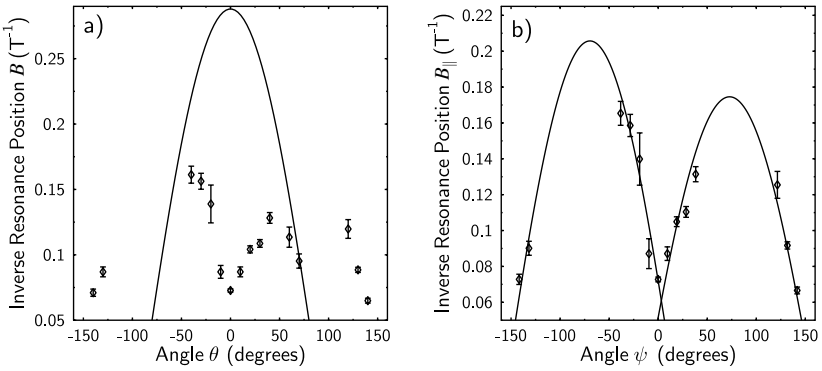

Figure 13. Resonance positions at $T = 1.5$ K and with $\phi = 20^\circ$ in different coordinate systems. (a) The resonance position versus angle θ in experimental coordinates. The solid line is the expected position of the feature associated with the superconducting-to-normal transition, which obscures the magneto-optical resonance at some angles. (b) The resonance position versus angle ψ in 'FTR' coordinates; the solid line is a fit to equation (19).

The $\phi = 0^\circ$ experimental coordinates $\boldsymbol{B}, \theta$ are identical with the FTR coordinates $\boldsymbol{B}_{||}, \psi$ because for this angle the magnetic field lies in the plane of the Fermi sheet (see figure 10). By contrast, the $\phi = 90^\circ$ data give only one point in 'FTR' coordinates because all resonance positions fall together at $\psi = 0^\circ$. The final figure, figure 14, is composed of all the resonances from all the azimuthal angles. In figure 14(a) the resonances are shown in experimental coordinates for many values of ϕ and the solid line is again the prediction of the position of the superconducting feature. Figure 14(b) shows the same data in transformed coordinates; in 'FTR' coordinates all of the resonance positions nicely map onto two arches, showing the origin of the resonance unambiguously.

The two arches in figure 14 have been fitted using equation (19). The fit parameters are shown in table 2; the column 'Total' gives the fitting results for all the resonances from different ϕ-angles fitted together in 'FTR' coordinates. A schematic diagram of the Q1D Fermi sheets of κ-(BEDT-TTF)$_2$Cu(NCS)$_2$ is plotted in figure 15, showing the interplane corrugation deduced from the FTR results; the warping is greatly exaggerated [6].

Table 2. The results from the fits of the κ-(BEDT-TTF)$_2$Cu(NCS)$_2$ FTR data shown in figure 14(b). The parameter $m^*_{1D} = e/A$ is defined by analogy with conventional cyclotron resonance; the maximum FTR angular frequency is $eB_{||}/m^*_{1D}$ (see equation (19)).

	ϕ	0°	20°	45°	Total
Left	A/ω_{1D} (T^{-1})	0.22 ± 0.01	0.21 ± 0.01	0.25 ± 0.01	0.221 ± 0.006
	ψ_0	$18.0^\circ \pm 1.7^\circ$	$20.4^\circ \pm 1.8^\circ$	$11.0^\circ \pm 1.7^\circ$	$17.3^\circ \pm 1.1^\circ$
	m^*_{1D} (m_e)	1.80 ± 0.08	1.92 ± 0.07	1.58 ± 0.08	1.79 ± 0.04
Right	A/ω_{1D} (T^{-1})	0.17 ± 0.01	0.18 ± 0.01	0.19 ± 0.01	0.173 ± 0.005
	ψ_0	$-20.4^\circ \pm 2.1^\circ$	$-17.2^\circ \pm 1.9^\circ$	$-18.7^\circ \pm 1.5^\circ$	$-19.4^\circ \pm 1.2^\circ$
	m^*_{1D} (m_e)	2.34 ± 0.11	2.26 ± 0.10	2.09 ± 0.09	2.29 ± 0.07

3.4. Summary

The magneto-optical techniques described in section 2 have enabled the corrugations of the Q1D Fermi-surface sheets in κ-(BEDT-TTF)$_2$Cu(NCS)$_2$ to be characterized unambiguously.

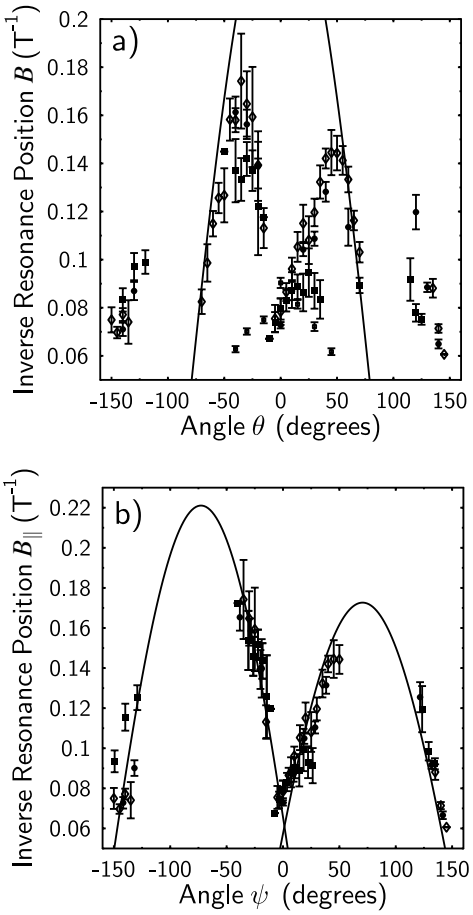

Figure 14. The resonance positions versus angle at 1.5 K for azimuthal angles $\phi = 0^\circ$, 20°, 45°, and 90° (diamonds, filled circles, filled squares, and open squares respectively). (a) Experimental coordinates, with the solid line representing the position of the superconducting feature. (b) The same data in 'FTR' coordinates, showing two arches. The solid line is a fit of the data points to equation (19).

Two corrugations were found; the directions of the corrugations of the Fermi sheet are 17.3° and -19.4° with respect to the reciprocal k_a-axis. It should be noted that the conventional methods for studying the Fermi-surface topology (those based on the de Haas–van Alphen and Shubnikov–de Haas effects) are unable to give such information [6].

FTRs are potentially observable in many substances with open Fermi-surface sections; the techniques described in this paper should be widely applicable.

4. Cyclotron harmonics in β''-(BEDT-TTF)$_2$SF$_5$CH$_2$CF$_2$SO$_3$

4.1. Introduction

We have already mentioned that a number of theories of superconductivity in charge-transfer salts [13, 14, 16] stress the importance of the details of the Fermi-surface topology in providing suitable prerequisites for superconductivity. In this context, the isostructural charge-transfer

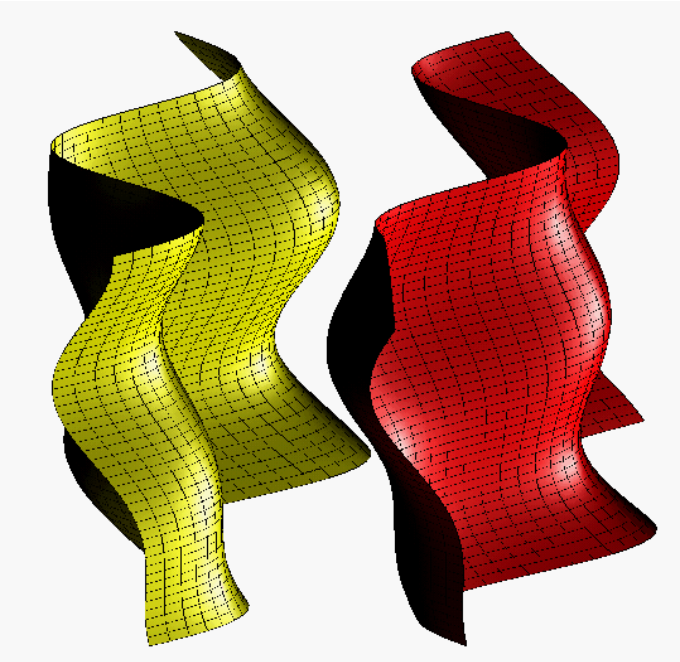

Figure 15. A schematic diagram of the quasi-one-dimensional Fermi sheets in κ-(BEDT-TTF)$_2$Cu(NCS)$_2$ with the single sinusoidal corrugation in the in-plane k_c-direction and the two newly discovered corrugations in the interplane direction.

salts β''-(BEDT-TTF)$_2$SF$_5$CH$_2$CF$_2$SO$_3$ and β''-(BEDT-TTF)$_2$AuBr$_2$ are of great potential interest. The predicted Fermi surfaces for the two salts are virtually identical, each consisting of a quasi-two-dimensional (Q2D) cylinder and a pair of warped sheets [54, 55]. However, whereas the former is a superconductor (indeed, the first entirely organic superconductor to be synthesized) with $T_c \approx 5.4$ K [54], the latter exhibits a series of magnetic field-dependent density-wave ground states at low temperatures [55]. It is therefore of great interest to derive accurate techniques for comparing the Fermi surfaces of the two β''-(BEDT-TTF) salts.

In this section, we report millimetre-wave magnetoconductivity measurements, using the techniques described in section 2, which allow the topology of the Q2D Fermi-surface sections of β''-(BEDT-TTF)$_2$SF$_5$CH$_2$CF$_2$SO$_3$ to be deduced with confidence. The data also show that the material possesses a Fermi surface which extends in the interplane direction. in contrast to recent theoretical suggestions [6, 9]. The millimetre-wave conductivity studies are analysed using a model which is able to predict the occurrence of cyclotron harmonics with good accuracy. Moreover, the millimetre-wave conductivity measurements give the first experimental evidence for a mass renormalization effect which has been recently predicted to occur in narrow-bandwidth metallic systems [8].

4.2. Experimental details

The high-frequency conductivity measurements were made using the resonant cavity techniques described in section 2. The β''-(BEDT-TTF)$_2$SF$_5$CH$_2$CF$_2$SO$_3$ sample (of size $\sim 0.5 \times 0.5 \times 0.1$ mm^3) was placed inside a rectangular cavity resonating in the TE$_{102}$ mode at 71.2 GHz [18]. As in the previous sections, the samples were aligned in the cavity such that

the oscillating $\boldsymbol{B}$-field is parallel to the highly conducting planes; induced currents must flow in the interplane (low-conductivity) direction, leading to a skin depth greater than the sample size. Since the conductivity anisotropy is large, the dissipation is dominated by the interplane conductivity [18, 27].

GHz conductivity studies were carried out for different orientations θ at $\phi = 105^\circ$, 75°, 45°, and 15°. Figure 16 shows field sweeps between 0 and 15 T at a fixed frequency of 71.2 GHz, for $\phi = 105^\circ$ and 45°. Only θ-angles between 0° and 70° are shown as the resonance positions are symmetrical about $\theta = 0^\circ$. The data have been normalized and offset for clarity. The feature at 2 T on all sweeps is a background of the apparatus [18]. At intermediate fields several broad resonances can be seen. For $\phi = 105^\circ$, one resonance moves to higher fields with increasing angle. The position of the resonance in magnetic field for different θ is fitted to

$$\frac{\omega}{B} = A\cos(\theta - \theta_0) \tag{24}$$

giving values $A/\omega = 0.175 \pm 0.005\ \mathrm{T}^{-1}$ and $\theta_0 = 2^\circ \pm 2^\circ$. This is consistent with the behaviour expected of a cyclotron resonance, where the resonance should be centred around $\theta_0 = 0^\circ$ [6].

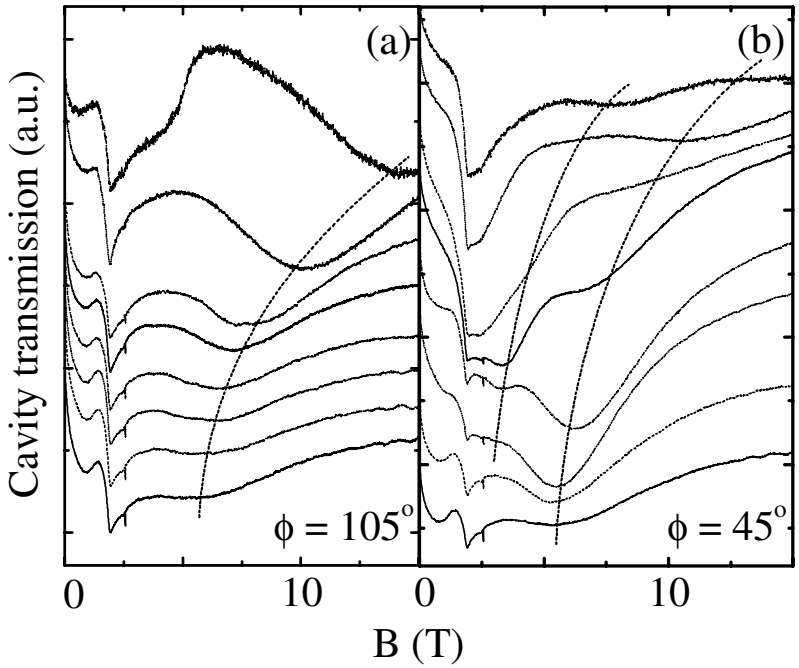

Figure 16. Transmission of the resonant cavity loaded with a single crystal of β''-(BEDT-TTF)$_2$SF$_5$CH$_2$CF$_2$SO$_3$ versus magnetic field for $\theta = 0^\circ$ (lowest traces) to $\theta = 70^\circ$ (uppermost traces) and azimuthal angles $\phi = 105^\circ$ (a) and $\phi = 45^\circ$ (b). The temperature is 1.5 K. The dotted lines are guides to the eye, and indicate the positions of the resonances.

At $\phi = 45^\circ$ (figure 16(b)) another resonance appears for higher θ at approximately half the field of the main resonance. This resonance is also seen for $\phi = 75^\circ$ and $\phi = 15^\circ$, and follows a $\cos\theta$ dependence of the inverse resonance field with fitting parameters $A/\omega = 0.36 \pm 0.01\ \mathrm{T}^{-1}$ and $\theta_0 = -1^\circ \pm 1^\circ$. The value of A/ω strongly suggests that this resonance is the second harmonic of the main cyclotron resonance. At some azimuthal angles an additional feature becomes visible at $\theta \sim 60^\circ$, behaving like a third harmonic of the cyclotron resonance.

4.3. Harmonics

Harmonics of cyclotron resonance in Q2D metals have been predicted by Blundell *et al* [49] and Hill [27]. Reference [49] predicts the presence of higher harmonics in the real-space velocity of charge carriers in cyclotron orbits about non-elliptical Fermi-surface cross-sections, leading to harmonics of the cyclotron resonance. However, this does not predict even harmonics.

By contrast, Hill [27] considers a cylindrical Fermi surface which is warped in the interplane direction; however, the warping vector is *not* directed along the cylinder axis. Second and third harmonics of the fundamental are predicted. However, we have proposed a new mechanism which predicts cyclotron harmonics and their angular behaviour without the need for a shifted warping vector [56]. Figure 17(a) shows the cross-section of a typical warped Q2D Fermi-surface section (warping greatly exaggerated). For a general orientation of $\boldsymbol{B}$, quasiparticles follow orbits about the Fermi surface such that the z-component of their real-space velocity, v_z, oscillates. If the angle θ is small, most orbits remain within one Brillouin zone in the k_z-direction and v_z oscillates at the cyclotron frequency ω_c. As θ increases, the orbits can extend over several Brillouin zones in the k_z-direction and v_z acquires oscillatory components at harmonics of ω_c. The largest amplitude of the ω_c-resonance will occur for an angle θ_1 in figure 17(a), as the change in v_z for orbits crossing one Brillouin zone will be greatest. The second harmonic will likewise be strongest at θ_2, and so on. Simple geometry leads to the following values for these angles [56]:

$$\tan\theta_1 = \frac{\pi/c}{k_F} \qquad \tan\theta_2 = 2 \times \frac{\pi/c}{k_F}. \tag{25}$$

Here $2\pi/c$ is the Brillouin-zone height in the interplane direction and $2k_F$ is the width of the Fermi-surface cross-section.

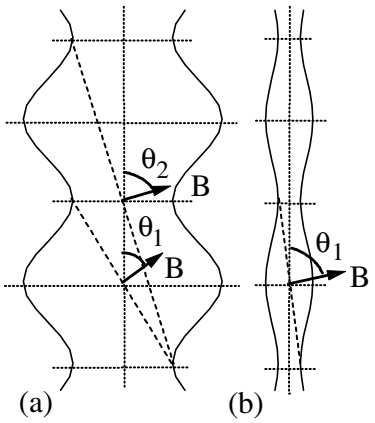

Figure 17. (a) and (b) represent two different cross-sections of a warped cylindrical Fermi surface. Cyclotron orbits about the Fermi surface are shown schematically as dotted lines for two inclinations of the magnetic field $\boldsymbol{B}$ to the cylinder axis, θ_1 and θ_2.

Figure 18(a) shows the intensities of the resonances at an azimuthal angle $\phi = 75^\circ$ as a function of the angle θ. The angle dependence of the resonance amplitude of the first harmonic has been fitted to a suitable functional form [56] centred on θ_1, and the angular behaviour of the second and third harmonics has been predicted using the same function but centred on θ_2 and θ_3 respectively.

The angle θ_1 depends on the anisotropy of the Fermi surface and its azimuthal orientation. Figures 17(a) and 17(b) represent rotating the field through the major and minor axes of the

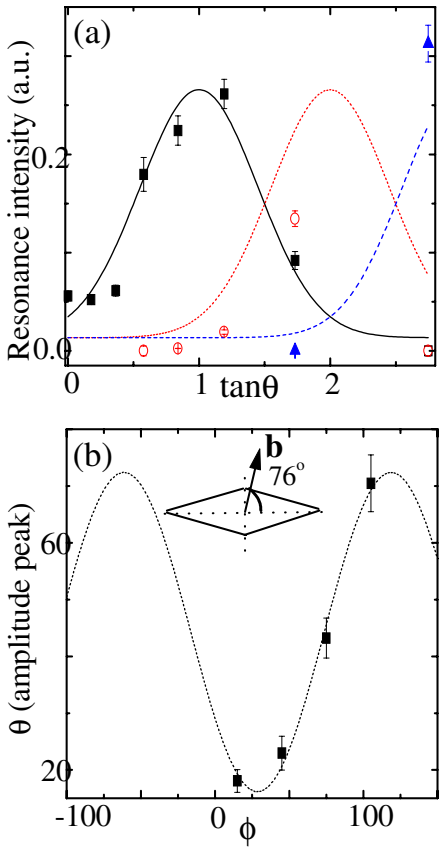

Figure 18. (a) Intensity of the cyclotron resonances versus θ for $\phi = 75^\circ$. The solid curve is the fit to the intensity of the fundamental cyclotron resonance, centred on angle θ_1; the square points are experimental data. The dotted curve is the predicted intensity of the second harmonic, centred on θ_2; the hollow circles are experimental data. The dashed curve is the predicted intensity of the third harmonic, centred on θ_3; corresponding experimental points are drawn as triangles. (b) The parameter θ_1 plotted as a function of ϕ; points are experimental values and the curve is a fit to equation (26). The inset shows the orientation of the Fermi-surface cross-section with respect to the crystal's k_b-axis (b^*-axis) derived from the fit.

Fermi-surface cross-section; in figure 17(b), θ_1 is much higher than for figure 17(a). The angle θ_1 should vary with rotation as

$$\theta_1 = \alpha + \gamma \cos 2(\phi + \phi_0) \tag{26}$$

where ϕ_0 is related to the orientation of the Fermi surface with respect to the crystal axes and α and γ are constants corresponding to the major and minor axes of the Fermi-surface cross-section. Figure 18(b) shows the values of θ_1 for the azimuthal orientations studied fitted to equation (26). From the maximum and minimum values of θ_1, the major and minor axes of the Fermi-surface cross-section are found to be in the ratio 10.5 ± 1.8:1, in very good agreement with the 9 ± 0.2:1 found from angle-dependent magnetoresistance oscillation (AMRO) data [57,58]. The fitted value of ϕ_0 is used to orientate the Fermi surface with respect to the crystal axes, as shown in figure 18(b), inset. The orientation of the major axis (inclined at an angle $76 \pm 4^\circ$ to the k_b-axis (b^*-axis)) agrees with orientations deduced from AMRO data [57,58] to within experimental errors.

Finally, we note that the observation of cyclotron harmonics which obey such an angle dependence strongly suggests that the interplane transport in β''-(BEDT-TTF)$_2$SF$_5$CH$_2$CF$_2$SO$_3$ is coherent, i.e. that the material has a three-dimensional Fermi surface (cf. reference [9]).

4.4. Masses

A cyclotron mass $m^*_{\rm CR} = 2.3 \pm 0.1\ m_{\rm e}$ was deduced from the angular frequency ω and magnetic field B of the fundamental resonance at $\theta = 0$ using the well-known formula [6]

$$\omega = \frac{eB}{m^*_{\rm CR}}. \tag{27}$$

Cyclotron resonance gives a different measure of the quasiparticle mass to that from a thermodynamic experiment such as one based on the de Haas–van Alphen effect [6, 17]; in the simplest theoretical picture [6, 17], the mass measured in the cyclotron resonance measurements represents the bare band mass renormalized by electron–phonon interactions, whereas the mass measured in the thermodynamic measurements is additionally renormalized by electron–electron interactions. In spite of a large number of magneto-optical experiments on BEDT-TTF salts (see reference [6] for a discussion), only two definitive reports of cyclotron resonance, both in α-(BEDT-TTF)$_2$NH$_4$Hg(SCN)$_4$, have been made [26,27]. In these studies, a cyclotron resonance corresponding to a mass of $m^*_{\rm CR} = 1.9\, m_{\rm e}$ was measured [26,27]; this may be compared with an effective mass from magnetic quantum oscillations of $m^* = 2.5\, m_{\rm e}$ [60]. The relative sizes of the two masses ($m^*_{\rm CR} < m^*$) is therefore in qualitative agreement with the theoretical predictions mentioned above. By contrast, in the current experiments on β''-(BEDT-TTF)$_2$SF$_5$CH$_2$CF$_2$SO$_3$, $m^*_{\rm CR} = 2.3 \pm 0.1 m_{\rm e}$; this may be compared with a mass $m^* = 2.0 \pm 0.1\ m_{\rm e}$ deduced from quantum oscillations [56, 59] (i.e. $m^*_{\rm CR} > m^*$). Thus it appears that the predictions of an enhancement of the effective mass derived from magnetic quantum oscillations over that measured in a cyclotron-resonance-like experiment do not necessarily hold. Hubbard-model calculations have recently been carried out [8] which contradict the simple theories and appear to support the above experimental observations. In these calculations it was found that the relationship between the two masses depends strongly on the characteristics of the material measured (e.g. band filling) and in some cases m^* can be exceeded by $m^*_{\rm CR}$.

4.5. Summary

In summary, we have performed experiments on β''-(BEDT-TTF)$_2$SF$_5$CH$_2$CF$_2$SO$_3$, showing that the Q2D section of the Fermi surface is highly elongated. Harmonics of cyclotron resonance have been seen in the millimetre-wave response of the sample and are explained by a new mechanism which confirms the elongation and orientation of the Fermi-surface cross-section. We have also found that in this material the effective mass determined from cyclotron resonance experiments is greater than that measured from magnetic quantum oscillations, in agreement with recent theoretical work.

5. Concluding remarks

We have described a novel resonant cavity system which allows the bulk magnetoconductivity of single crystals of anisotropic metals to be measured at GHz frequencies. The cavity permits detailed studies of the dependence on the magnetic field orientation of the high-frequency magnetoconductivity.

The apparatus has been used to measure details of the Fermi-surface topology of two organic superconductors; many of the details revealed are inaccessible to conventional fermiological techniques such as the de Haas–van Alphen effect approach. Moreover, the technique is able to give information about many-body effects and the coherence (or lack of it) of the interplane transport. It is hoped that the publication of this information will encourage similar measurements elsewhere, and the application of the technique to other systems.

Acknowledgments

We are very grateful indeed to Bill Hayes, who has encouraged and supported this work from the very beginning, and offered valuable advice to all of us. One of us (JS) would also like to thank Bill for encouraging him in 1987 to 'go and try some high-field experiments on these BEDT-TTF crystals'; the research group has benefited greatly from this suggestion! We should also like to thank Terry Holliday and Mark Witney for technical assistance. Work on organic molecular metals at Oxford is supported by EPSRC. NHMFL Tallahassee is supported by the Department of Energy, the National Science Foundation, and the State of Florida.

References

[1] Kino H and Fukuyama H 1996 *J. Phys. Soc. Japan* **65** 2158
McKenzie R 1998 *Comment. Condens. Matter Phys.* **18** 309
Strong S P, Clarke D G and Anderson P W 1994 *Phys. Rev. Lett.* **73** 1007
Vescoli V, Degiorgi L, Henderson W, Grüner G, Starkey K P and Montgomery L K 1998 *Science* **281** 1181
[2] Orenstein J and Millis A J 2000 *Science* **288** 468
Anderson P W 2000 *Science* **288** 480
[3] Maeno Y *et al* 1994 *Nature* **372** 532
Luke G M *et al* 1998 *Nature* **394** 558
Mackenzie A P *et al* 1998 *Phys. Rev. Lett.* **80** 161
Ishida K *et al* 1998 *Nature* **396** 658
[4] Ardavan A, Edwards R S, Rzepniewski E, Singleton J and Blundell S J 2001 *Proc. Conf. on Research in High Magnetic Fields (Porto, August 2000); Physica* B at press
[5] Ramirez A P 1997 *J. Phys.: Condens. Matter* **9** 8171
Rao C N R 1999 *J. Mater. Chem.* **9** 1
Tokura Y and Nagaosa N 2000 *Science* **288** 462
[6] Singleton J 2000 *Rep. Prog. Phys.* **63** 1111
[7] Laughlin R B, Lonzarich G G, Monthoux P and Pines D 2001 *Phys. Rev. Lett.* submitted
[8] Kanki K and Yamada K 1997 *J. Phys. Soc. Japan* **66** 1103
[9] Moses P and McKenzie R H 1999 *Phys. Rev.* B **60** 7998
Yoshioka D 1995 *J. Phys. Soc. Japan* **64** 3168
McKenzie R H 1999 *Preprint* cond-mat/9905044
Merino J and McKenzie R H 1999 *Preprint* cond-mat/9909041 (2 September)
[10] Carrington A, Bonalde I J, Prozorov R, Gianetta R W, Kini A M, Schlueter J, Wang H H, Geiser U and Williams J M 1999 *Phys. Rev. Lett.* **83** 4172
[11] Elsinger H, Wosnitza J, Wanka S, Hagel J, Schweitzer D and Strunz W 2000 *Phys. Rev. Lett.* **84** 6098
[12] Ichimura K *et al* 1999 *Synth. Met.* **103** 1812
Ichimura K *et al* 1999 *J. Supercond.* **12** 519
Ichimura K *et al* 2001 *Proc. Int. Conf. on the Science and Technology of Synthetic Metals (Bad Gastein, July 2000); Synth. Met.* at press
[13] Schmalian J 1998 *Phys. Rev. Lett.* **81** 4232
[14] Kuroki K and Aoki H 1999 *Phys. Rev.* B **60** 3060
[15] Maki K, Puchkaryov E and Won H 1999 *Synth. Met.* **103** 1933
[16] Louati R, Charfi-Kaddour S, Ben Ali A, Bennaceau R and Heritier M 1999 *Synth. Met.* **103** 1857
[17] Quader K F, Bedell K S and Brown G E 1987 *Phys. Rev.* B **36** 156
Leggett A J 1968 *Ann. Phys., NY* **46** 76

Kohn W 1961 *Phys. Rev.* **123** 1242
[18] Ardavan A, Schrama J M, Blundell S J, Singleton J, Hayes W, Goy P, Kurmoo M and Day P 1998 *Phys. Rev. Lett.* **81** 713
[19] Ardavan A, Blundell S J and Singleton J 1999 *Phys. Rev.* B **60** 15 500
[20] Produced by AB Millimetre, 52 Rue Lhomond, 75005, Paris, France. See www.abmillimetre.com for technical details.
[21] Schrama J M, Rzepniewski E, Ardavan A, Edwards R, Singleton J, Kurmoo M and Day P 1999 *Proc. EOS/SPIE Int. Symp. on Terahertz Spectroscopy (Munich, 1999); Proc. SPIE* **3828** 311
[22] Hewson A C 1993 *The Kondo Problem to Heavy Fermions* (Cambridge: Cambridge University Press)
Haanappel E G 1998 *Physica* B **246+247** 78 and references therein
[23] For a recent collection of relevant literature, see
Risborough P S 1998 *Physica* B **246+247** 378
[24] Cole B E, Peeters F M, Ardavan A, Hill S O, Singleton J, Batty W, Chamberlain J M, Polisskii A, Henini M and Cheng T 1997 *J. Phys.: Condens. Matter* **9** 3163
[25] The skin depth ($\delta = (\pi\sigma f\mu)^{-1/2}$) is a measure of how far electromagnetic waves of frequency f travel into a sample of permeability μ and conductivity σ before their amplitude is attenuated by a factor e^{-1}. Elemental metals usually have skin depths of a fraction of a micron at GHz frequencies and room temperature. See e.g.
Bleaney B I and Bleaney B 1990 *Electricity and Magnetism* (Oxford: Oxford University Press) p 236
[26] Polisskii A, Singleton J, Goy P, Hayes W, Kurmoo M and Day P 1996 *J. Phys. C: Solid State Phys.* **8** L195
[27] Hill S 1997 *Phys. Rev.* B **55** 4931
Hill S, Brooks J S, Qualls J S, Burgin T, Fravel B, Montgomery L K, Sarrao J and Fisk Z 1998 *Physica* B **110** 246
[28] Mola M, Hill S, Goy P and Gross M 2000 *Rev. Sci. Instrum.* **71** 186
[29] Dressel M, Klein O, Grüner G, Carlson K D, Wang H H and Williams J M 1994 *Phys. Rev.* B **50** 13 603
[30] Ishiguro T, Yamaji K and Saito G 1998 *Organic Superconductors (Springer Series in Solid-State Sciences vol 88)* 2nd edn (Berlin: Springer) p 149
[31] Schrama J M, Rzepniewski E, Edwards R, Singleton J, Ardavan A, Kurmoo M and Day P 1999 *Phys. Rev. Lett.* **83** 3041
[32] Ohta H, Yamamoto Y, Akioka K, Motokaw M, Sasaki T and Fukase T 1997 *Synth. Met.* **86** 2011
[33] Demishev S V, Semeno A V, Sluchanko N E, Samarin N A, Vosboinikov I B, Glushkov V V, Singleton J, Blundell S J, Hill S O, Hayes W, Kartsovnik M V, Kovalev A E, Kurmoo M, Day P and Kushch N D 1996 *Phys. Rev.* B **53** 12 794
[34] Singleton J, Pratt F L, Doporto M, Janssen T J B M, Kurmoo M, Perenboom J A A J, Hayes W and Day P 1992 *Phys. Rev. Lett.* **68** 2500
[35] Poole C P 1967 *Electron Spin Resonance* (New York: Interscience) ch 8
[36] Bleaney B I and Bleaney B 1990 *Electricity and Magnetism* (Oxford: Oxford University Press) p 293
[37] Klein O, Donovan S, Dressel M and Grüner G 1993 *Int. J. Infrared Millimeter Waves* **14** 2423
[38] Caulfield J M, Lubczynski W, Pratt F L, Singleton J, Ko D Y K, Hayes W, Kurmoo M and Day P 1994 *J. Phys.: Condens. Matter* **6** 2911
[39] Harrison N, Caulfield J, Singleton J, Reinders P H P, Herlach F, Hayes W, Kurmoo M and Day P 1996 *J. Phys.: Condens. Matter* **8** 5415
[40] Mielke C M, Harrison N, Rickel D G, Lacerda A H, Vestal R M and Montgomery L K, 1997 *Phys. Rev.* B **56** R4309
[41] Kartsovnik M V, Logvenov G Yu, Ishiguro T, Biberacher W, Anzai H and Kushch N D 1996 *Phys. Rev. Lett.* **77** 2530
[42] Kartsovnik M V, Logvenov G Yu, Ito H, Ishiguro T and Saito G 1995 *Phys. Rev.* B **52** R15 715
[43] Sasaki T, Biberacher W, Neumaier K, Hehn W, Andres K and Fukase T 1998 *Phys. Rev.* B **57** 10 889
[44] Oshima K, Mori T, Inokuchi H, Urayama H, Yamochi H and Saito G 1988 *Phys. Rev.* B **38** 938
[45] Sasaki T, Sato H and Toyota N 1990 *Solid State Commun.* **76** 507
Sasaki T, Sato H and Toyota N 1991 *Physica* C **185** 2687
[46] Kartsovnik M V, Kovalev A E, Laukhin V N, Ito H, Ishiguro T, Kushch N D, Anzai H and Saito G 1995 *Synth. Met.* **70** 819
[47] Nam M S, Honold M M, Harrison N, Mielke C H, Blundell S J, Singleton J, Kurmoo M and Day P 1999 *Synth. Met.* **103** 1905
[48] Blundell S J and Singleton J 1996 *J. Physique.* I **6** 1837
[49] Blundell S J, Ardavan A and Singleton J 1997 *Phys. Rev.* B **55** 6129
[50] Nam M S, Symington J A, Singleton J, Blundell S J, Ardavan A, Perenboom J A A J, Kurmoo M and Day P 1999 *J. Phys.: Condens. Matter* **11** L477

[51] Singleton J, Symington J A, Nam M S, Ardavan A, Kurmoo M and Day P 2000 *J. Phys.: Condens. Matter* **12** L641
[52] Shibauchi T *et al* 1997 *Phys. Rev.* B **55** R11 977
[53] Hill S, Uji S, Sandhu P S, Brooks J S and Seger L 1997 *Synth. Met.* **86** 1955
[54] Geiser U, Schluter J A, Wang H H, Kini A M, Williams J M, Sche P P, Zakowicz H I, VanZile M L, Dudek J D, Nixon P G, Winter R W, Gard G L, Ren J and Whangbo M-H 1996 *J. Am. Chem. Soc.* **118** 9996
[55] House A A, Harrison N, Blundell S J, Deckers I, Singleton J, Herlach F, Hayes W, Perenboom J A A J, Kurmoo M and Day P 1996 *Phys. Rev.* B **53**
[56] Edwards R S, Ardavan A, Rzepniewski E and Singleton J 2001 submitted
[57] Nam M S, Blundell S J, Ardavan A, Symington J A and Singleton J 2001 *J. Phys.: Condens. Matter* **13** 2271
[58] Wosnitza J, Wanka S, Qualls J S, Brooks J S, Mielke C H, Harrison N, Schlueter J A, Williams J M, Nixon P G, Winter R W and Gard G L 1999 *Synth. Met.* **103** 2000
[59] Wosnitza J, Wanka S, Hagel J, Balthes E, Harrison N, Schlueter J A, Kini A M, Geiser U, Mohtasham J, Winter R W and Gard G L 2000 *Phys. Rev.* B **61** 7383
Wanka S, Hagel J, Beckmann D, Wosnitza J, Schlueter J A, Williams J M, Nixon P G, Winter R W and Gard G L 1998 *Phys. Rev.* B **57** 3084 and references therein
[60] Doporto M, Pratt F L, Singleton J, Kurmoo M and Hayes W 1992 *Phys. Rev. Lett.* **69** 991